

Collision Trajectories in Hill's Problem: Application to the Mars-Deimos System

Yehonatan Or-Hof

Research Project under the guidance of Prof. Pini Gurfil
and Dr. Alexander Batkhin

Department of Aerospace Engineering
Technion – Israel Institute of Technology
Haifa 3200003, Israel

Abstract

This work presents a methodology for detecting collision trajectories with the secondary mass in Hill's three-body problem, applied to the Mars-Deimos system. The inherent singularity at the collision point is alleviated by employing the Levi-Civita regularization, which transforms the equations of motion into a nonsingular form. A systematic search for collision trajectories was performed by numerically integrating the regularized equations backward in fictitious time from the center of the secondary body. The investigation spanned a range of Jacobi constants and initial collision angles. Trajectory data was subsequently transformed into the Hill rotating frame, and Deimos' physical rotating frame. The results indicate that a Jacobi constant of $C = 3.76$ yields a particularly large set of escape/collision trajectories for a relatively low energy. A further investigation was conducted for $C = 3.76$ by identifying a trajectory that meets the condition of minimizing impact velocity.

1 Introduction

Orbital mechanics as a field of study traces its origins to the early 17th century, when Johannes Kepler used Tycho Brahe’s detailed astronomical data to formulate his laws of planetary motion [1], which describe the motion of two celestial bodies. This marked a key shift from descriptive astronomy to a predictive physical science. Sir Isaac Newton later provided the theoretical foundation in his *Principia* (1687) [2], introducing the laws of motion and the law of universal gravitation. Among other things, Newton described an attempt to understand the motion of the moon, which is considered the first investigation into the three-body problem.

Whereas the two-body problem described by Kepler’s laws is an integrable problem with an exact analytical solution, the general N-body problem, involving three or more bodies, lacks such a solution, and the system is known for its richness and diversity.

The first attempt to find a particular solution to the three-body problem was done by Euler [3], who also formulated the well-known circular restricted three-body problem (CR3BP). The CR3BP is a significant simplification of the general three-body problem. This model considers the motion of an infinitesimal third mass under the gravitational influence of two primary masses, which are in a circular orbit around their common center of mass (barycenter). Soon after, Lagrange discovered the triangular equilibrium points of the CR3BP [4].

Following Euler and Lagrange, Jacobi found a first integral of the circular restricted three-body problem in a synodic frame [5]. Hill recognized that, by using the Jacobian integral, there exist regions in the rotating frame wherein the massless body cannot enter. The boundary between the forbidden regions and the accessible regions is a zero-velocity curve [6].

Another important model for the restricted three-body problem was formulated to analyze the motion of the Moon with respect to Earth [7]. This model, referred to as Hill’s circular restricted three-body problem (HCR3BP), reformulated the CR3BP model for the case where the primary’s mass is significantly larger than the other two bodies.

In 1893, Henri Poincaré published his book *Les méthodes nouvelles de la mécanique céleste* [8], which contributed significantly to the understanding of the three-body problem. Poincaré’s work, together with that of Heinrich Bruns, proved that there is no general analytical solution for the three-body problem. Moreover, Poincaré determined the unpredictable nature of the dynamics, which laid the foundation for chaos theory.

A marked characteristic of Hill’s problem is that the resulting equations of motion, when appropriately scaled and viewed in rotating coordinates centered at the secondary mass, become independent of the specific mass ratio of the primaries [9]. This normalization allows the dynamical analysis to be generalized across various systems exhibiting a similar mass hierarchy.

The HCR3BP model has been used for the investigating of periodic orbits [9–12],

finding periodic orbits under perturbations such as solar radiation and oblateness [13–15], studying the dynamics of satellites [16], modeling the dynamics of star clusters [17], and detecting collision and escape trajectories [18]. Conley coined the term *low energy transient orbits* [19]. These transient orbits, which are orbits moving from a region dominated by one gravitational body to another, must pass near the collinear Lagrange points. Villac and Scheeres studied low-energy transient orbits in the Hill frame [20], and numerically found low-energy escape trajectories using a Poincaré surface of section (SoS) in the Hill frame.

The main objective of the current study is to identify trajectories that impact the secondary body under the dynamics of Hill’s problem. By identifying such collision trajectories, low-thrust guidance can be subsequently used for energy-efficient rendezvous with the secondary celestial body [21]. While numerous applications for such collision trajectories can be identified, this study focuses on the Mars-Deimos system. In this application scenario, Mars is treated as the primary and Deimos as the secondary, for which collision trajectories are found. This physical system is particularly well-suited for analysis under the Hill problem approximation due to its mass hierarchy [22–24].

The motivation for finding low-thrust, fuel-efficient collision orbits with Deimos stems from several reasons. The origin of Phobos and Deimos is still an open question [22, 25]. Whereas multiple missions have made observations of these celestial bodies, no spacecraft has ever landed on a Martian moon. Moreover, these bodies are recognized as having a high potential value for Mars exploration and for future human missions to Mars [26, 27], with applications including telecommunications, transportation, and infrastructure services.

The methodology for finding the collision orbits includes simulating the differential equations of Hill’s problem backward in time starting from the coordinate system’s origin, which is located at the center of mass of the secondary body. Due to the inherent singularity at the origin, the Levi-Civita regularization [28] was implemented. It is well known that for a collision trajectory to move from one Hill region to another, the zero-velocity curves (ZVC) must open in the vicinity of the Lagrange points. Thus, by integrating backward in time, only trajectories that pass through the vicinity of these points are considered applicable trajectories.

2 Model Formulation

2.1 The Circular Restricted Three-Body Problem

We consider the motion of a massless body S in the gravitational field of two primary bodies, P_1 and P_2 , which are in a circular orbit around their common barycenter. It is common to use normalized units such that the gravitational constant is 1, and the orbital period is 2π . A barycentric synodic coordinate system is defined such that the primaries

are fixed on the x -axis, as shown in Figure 1.

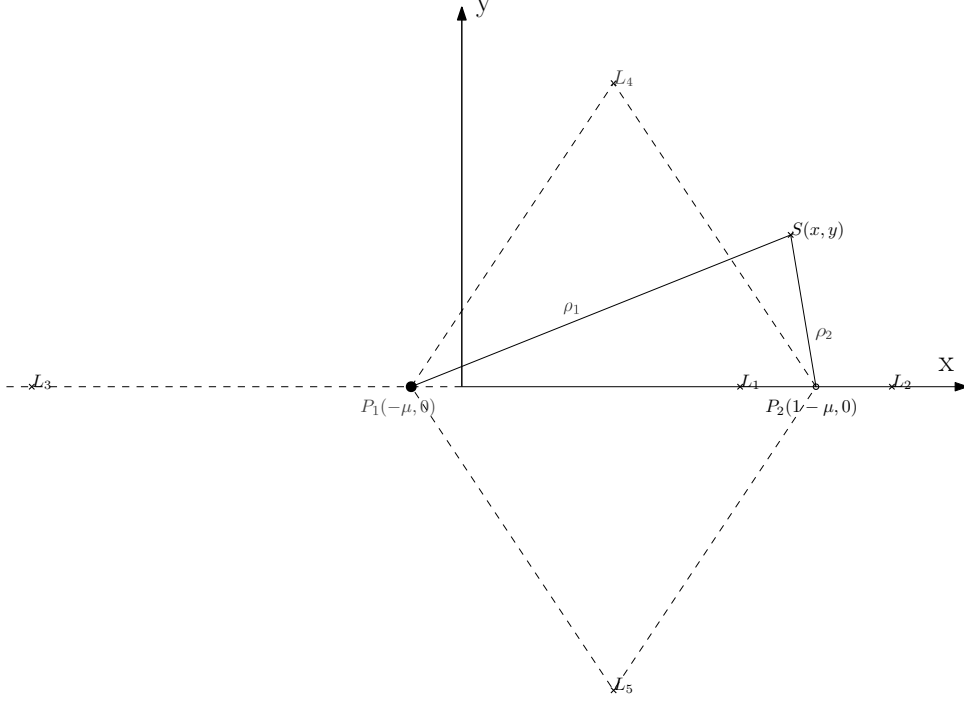


Figure 1: Synodic coordinates for the planar circular restricted three body problem

Let $\mu = m_2/(m_1 + m_2) \in (0, \frac{1}{2})$, where m_1 and m_2 are the masses of P_1 and P_2 , respectively. Moreover, $\rho_1 = ((x + \mu)^2 + y^2)^{\frac{1}{2}}$ and $\rho_2 = ((x - 1 + \mu)^2 + y^2)^{\frac{1}{2}}$ are the distances from S to P_1 and P_2 , respectively.

In this configuration, the normalized planar CR3BP equations of motion, describing the motion of S under the mutual gravitational forces of the primaries, are given by [29]

$$\ddot{x} = 2\dot{y} + x - (1 - \mu) \frac{x + \mu}{\rho_1^3} - \mu \frac{x - 1 + \mu}{\rho_2^3}, \quad (1a)$$

$$\ddot{y} = -2\dot{x} + y - \left(\frac{1 - \mu}{\rho_1^3} + \frac{\mu}{\rho_2^3} \right) y. \quad (1b)$$

In this framework, the five Lagrangian libration points, are denoted by (L_i) [29]. The points (L_1, L_2, L_3) are aligned collinear with the primaries. The remaining points (L_4, L_5) form an equilateral triangle with P_1, P_2 ; thus L_4 and L_5 are located at $(\frac{1}{2} - \mu, \pm \frac{\sqrt{3}}{2})$. The position of the collinear is given by the equation [29].

$$L_1 : x - \frac{1 - \mu}{(x + \mu)^2} + \frac{\mu}{(x - 1 + \mu)^2} = 0 \quad (2a)$$

$$L_2 : x - \frac{1 - \mu}{(x + \mu)^2} - \frac{\mu}{(x - 1 + \mu)^2} = 0 \quad (2b)$$

$$L_3 : x + \frac{1 - \mu}{(x + \mu)^2} + \frac{\mu}{(x - 1 + \mu)^2} = 0 \quad (2c)$$

The Hamiltonian of the planar CR3BP is given by [10, 29, 30]

$$H = \frac{1}{2}(p_x^2 + p_y^2) - \frac{1-\mu}{\rho_1} - \frac{\mu}{\rho_2} + p_x y - p_y x \quad (3)$$

where the momenta are $p_x = \dot{x} - y$ and $p_y = \dot{y} + x$. The dynamics are constrained by the Jacobi integral C , a constant of motion defined by

$$C = -2H = 2\Omega - (\dot{x}^2 + \dot{y}^2) \quad (4)$$

2.2 Hill's Approximation

Hill's problem is a limiting case of the CR3BP, which describes the dynamics in the vicinity of the secondary, P_2 , when $\mu \rightarrow 0$ [7, 9]. By shifting the coordinate system origin to P_2 , applying a scaling transformation of the coordinates (x, y) by $\mu^{\frac{1}{3}}$, and performing a Taylor-series expansion [31], the Hamiltonian becomes

$$H = \frac{1}{2}(p_x^2 + p_y^2) + p_x y - p_y x - x^2 + \frac{1}{2}y^2 - \frac{1}{(x^2 + y^2)^{\frac{1}{2}}} \quad (5)$$

Hill's circular restricted three-body problem (HCR3BP) was proven to be non-integrable [32], similarly to the CR3BP. The effective potential of the HCR3BP is defined as

$$\Omega(x, y) \triangleq \frac{3}{2}x^2 + \frac{1}{\sqrt{x^2 + y^2}} \quad (6)$$

The corresponding equations of motion are given by [29]

$$\ddot{x} - 2\dot{y} = \frac{\partial \Omega}{\partial x} = 3x - \frac{x}{r^3} \quad (7a)$$

$$\ddot{y} + 2\dot{x} = \frac{\partial \Omega}{\partial y} = -\frac{y}{r^3} \quad (7b)$$

where $r = \sqrt{x^2 + y^2}$. The Jacobi constant Hill's problem is given by

$$C = \frac{1}{2}(\dot{x}^2 + \dot{y}^2) - \frac{3}{2}x^2 - 1/r \quad (8)$$

Figure 2 depicts the coordinates of Hill's problem, wherein the secondary P_2 is positioned at the origin, and the primary is effectively moved to minus infinity as a result of the coordinate scaling transformation [10].

2.2.1 Lagrangian Points and Zero-Velocity Curves

Whereas the CR3BP is known for its five Lagrangian points [29], the HCR3BP dynamical system comprises only two, with the other equilibrium points eliminated due to the ap-

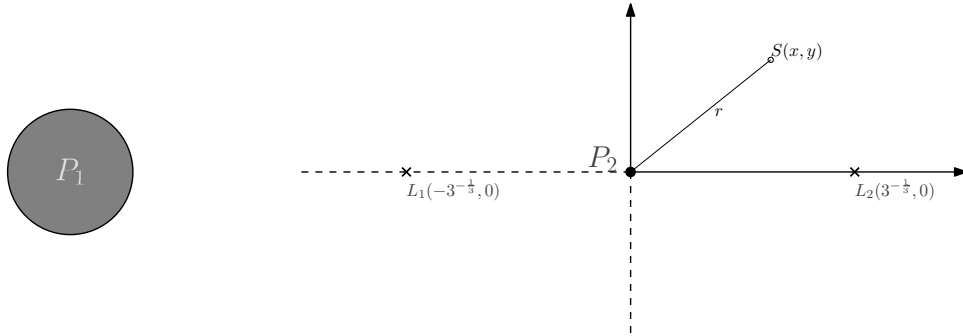


Figure 2: The coordinate system for Hill's circular restricted three body problem

proximation process [10]. The surviving equilibrium points are the collinear Lagrangian points L_1 and L_2 , located at $x = \pm(1/3)^{1/3}$ on the x -axis [29]. The boundaries of accessible motion are defined by the zero-velocity curves (ZVC) [19], given by the condition $2\Omega(x, y) = C$. For $C > 3^{4/3} \triangleq C^*$, the ZVC form a closed region around the secondary, trapping the particle; hence, no collision trajectory passing between the Hill regions can be found. As C decreases to the critical value $C^* = 3^{4/3}$, the ZVC open at L_1 and L_2 , creating passages that allow for escape or capture trajectories.

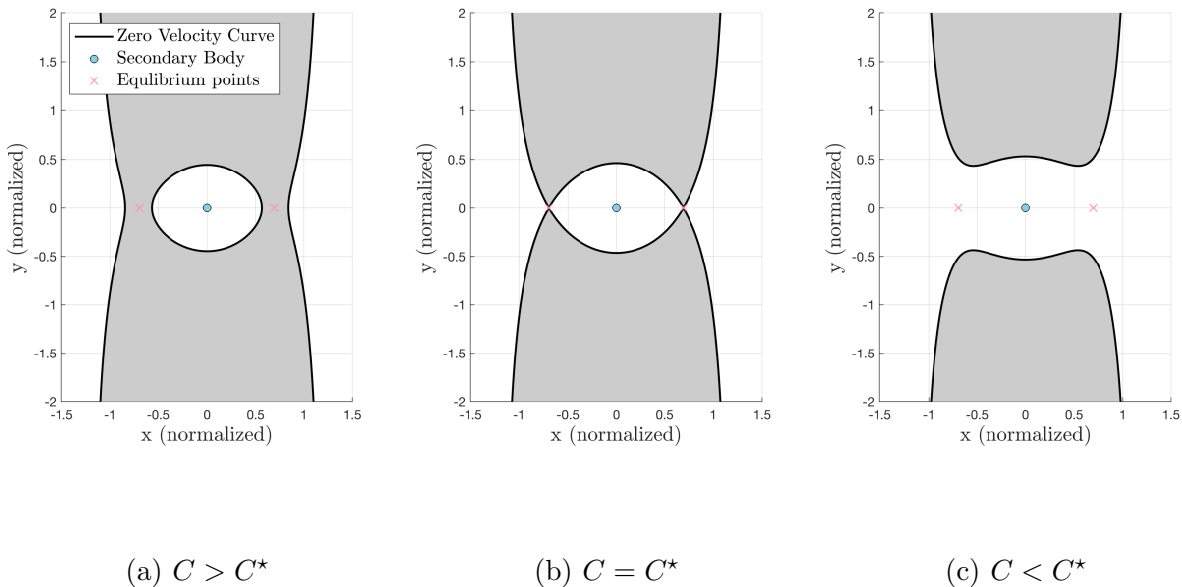


Figure 3: Zero-velocity curves for different values of the Jacobi constant C .

2.2.2 Inherent Symmetries

Another widely-discussed properties of the HCR3BP are fundamental symmetries, which simplify the analysis [10, 20, 29]. Let $\zeta = (x, y, \dot{x}, \dot{y})$ denote a valid solution to Eqs. (7).

Then, the following symmetries hold:

$$\zeta = (x, y, \dot{x}, \dot{y}) \xrightarrow{S_1} \zeta_{S_1} = (-x, y, \dot{x}, -\dot{y}) \quad (9a)$$

$$\zeta = (x, y, \dot{x}, \dot{y}) \xrightarrow{S_2} \zeta_{S_2} = (x, -y, -\dot{x}, \dot{y}) \quad (9b)$$

$$\zeta = (x, y, \dot{x}, \dot{y}) \xrightarrow{S_3} \zeta_{S_3} = (-x, -y, -\dot{x}, -\dot{y}) \quad (9c)$$

Moreover, due to the lack of explicit time dependence in the dynamical in the synodic frame, an important symmetry concerning time t arises: a solution traced back in reverse time also constitutes a valid solution,

$$\zeta = (x, y, \dot{x}, \dot{y}, t) \xrightarrow{S_t} \zeta_{S_t} = (x, y, \dot{x}, \dot{y}, -t) \quad (10)$$

2.3 Levi-Civita Regularization

To handle the singularity in the equations of motion at the origin ($r = 0$), we apply the Levi-Civita regularization [28] [33] [29]. Let us introduce new variables u, v in the complex plane. We use the complex transformation $z = f(\omega) = \omega^2$, where $z = x + iy$ and $\omega = u + iv$. This gives the coordinate transformation

$$x + iy = (u + iv)^2, \quad x = u^2 - v^2, \quad y = 2uv \quad (11)$$

The Levi-Civita transformation introduces a fictitious time τ related to the physical time t through

$$d\tau = \frac{dt}{4(u^2 + v^2)} \quad (12)$$

This transformation converts the equations of motion into the nonsingular, harmonic-oscillator form [29]

$$u'' - 8(u^2 + v^2)v' = \frac{\partial \tilde{\Omega}}{\partial u} = 4u [3(u^2 - v^2)(3u^2 + v^2) - C] \quad (13)$$

$$v'' + 8(u^2 + v^2)u' = \frac{\partial \tilde{\Omega}}{\partial v} = -4v [3(u^2 - v^2)(3u^2 + v^2) + C] \quad (14)$$

where

$$\tilde{\Omega}(u, v) \triangleq \left[\frac{3}{2}x^2 + \frac{1}{r} - \frac{C}{2} \right] |f'(\omega)|^2 = 6(u^2 + v^2)(u^2 - v^2)^2 + 4 - 2C(u^2 + v^2) \quad (15)$$

and $(\cdot)'$ denotes differentiation with respect to τ .

Thus, the singularity in origin is eliminated, and $\Omega(0, 0) = 4$. Moreover, applying the regularization transformation (11) to the expression of the Jacobi integral (8) yields the

regularized Jacobian integral [29]

$$\tilde{C} = (u')^2 + (v')^2 = 2\tilde{\Omega}(u, v) \quad (16)$$

Another useful observation pertains to the regularized velocity of the collision trajectories crossing the origin, which satisfies

$$u'(0)^2 + v'(0)^2 = 8 \quad (17)$$

The collision angle α is defined as the angle of the fictitious velocity vector with respect to the u -axis. Hence, the velocity components in the regularized coordinates can be expressed by

$$u'(0) = \sqrt{8} \cos(\alpha), \quad v'(0) = \sqrt{8} \sin(\alpha) \quad (18)$$

3 Numerical Search

The identification of collision trajectories in the HCR3BP requires a systematic numerical search, due to the absence of analytical solutions. A direct, forward integration approach is computationally inefficient, as it requires a trial-and-error search over a large four-dimensional space of initial conditions. A more efficient way is to use backward integration.

To find collision trajectories, the numerical integration starts precisely at the origin of the system, a strategy that is possible due to the Levi-Civita regularization. This reduces the search space for initial conditions to only two parameters: The Jacobi constant C and the collision angle α , as given in Eq. (18).

A systematic grid search was performed over this two-dimensional parameter space. The Jacobi constant was varied from $C = 3.5$ to $C = 4.3$, a range where the ZVC are open. The collision angle was varied from $\alpha = 0[\text{deg}]$ to $179[\text{deg}]$. Due to the inherent symmetries of the Hill problem as given by Eqs. (9), this range covers all unique trajectory geometries. For each pair (C, α) , the regularized equations of motion (13) were numerically integrated using an eighth-order explicit Runge-Kutta solver, with adaptive step-size control [34]. Table 1 shows the values used in this numerical search.

Parameter	Value
Jacobi constant range	[3.5, 4.3]
Collision angle range	[0, 179] <i>deg</i>
Jacobi constant search interval	0.01
Collision angle search interval	0.1 <i>deg</i>
Final fictitious time	10 (dimensionless)
Initial velocity magnitude ($u - v$ plane)	$\sqrt{8}$

Table 1: Parameters for the numerical search

In addition to terminating the integration at a maximum fictitious time, τ_{final} , two event-based termination conditions were implemented to improve computational efficiency and ensure the physical validity of the trajectories.

First, the backward integration was terminated if a trajectory reached a large boundary in the regularized plane, defined by $\sqrt{u^2 + v^2} = 3$. Because the HCR3BP is a local approximation, trajectories that travel this far from the secondary are considered physically invalid. Second, trajectories that returned to the origin of the regularized frame, $(u, v) = (0, 0)$, were omitted. In the context of backward integration from a collision, a return to the origin represents a trajectory that connects one collision to another without ever leaving the immediate vicinity of the secondary. Physically, these are purely local orbits that do not cross the Hill sphere boundary and thus do not qualify as escaping trajectories [20].

3.1 Mission Design Considerations

The dynamical framework of Hill’s problem is applicable to multiple celestial systems including the Mars-Deimos system. To investigate trajectories within this system, it is necessary to identify the subset of solutions that are constrained to a single collision with Deimos. Although Deimos is highly nonspherical, for this procedure, the mean radius of Deimos was used, as given in Table 2, which shows the physical and dynamical properties of the system. We refer to the single-collision criterion as Criterion 1.

Parameter		Value
<i>Physical Properties</i>		
Mass of Mars	M	6.4169×10^{23} kg
Mass of Deimos	m	1.4413×10^{15} kg
Mean radius of Deimos	R_{Deimos}	6.27 km
Deimos fit ellipsoid		$8.04 \times 5.89 \times 5.11$ km
<i>Deimos Orbital Parameters</i>		
Semi-major Axis	a	23,457.5 km
Eccentricity	e	0.0003
Orbital Period	T	1.09×10^5 s (≈ 30.3 hr)
<i>Physical Constant</i>		
Newtonian constant of gravitation	G	$6.67430 \times 10^{-11} \frac{\text{m}^3}{\text{kg}\cdot\text{s}^2}$

Table 2: Physical and dynamical parameters for the Mars-Deimos system

Another criterion for removing infeasible trajectories was applied based on the established principle that, in the CR3BP, transient orbits must pass through the vicinity of the equilibrium points [19]; we refer to this criterion as Criterion 2. Because the HCR3BP is a limiting case of the CR3BP, the same principle applies. Therefore, any simulated

trajectory that did not pass the vicinity of L_1 or L_2 , ($|x_{max}| \leq (1/3)^{1/3}$) was considered physically infeasible, and was removed from the final analysis.

We use the term *applicable trajectories* for trajectories that follow both criterion 1 (the single-collision criterion), and Criterion 2 (passing through the vicinity of the equilibrium points).

Figure 4 shows the number of applicable trajectories as a function of the Jacobi constant. As can be seen in Fig. 4, for an increment of 0.1 deg, no escape trajectories were found for $C \geq 3.79$. Moreover, $C = 3.76$ provides a unique combination of a large number of collision trajectories with a relatively low amount of energy, rendering this Jacobi constant useful for further investigation.

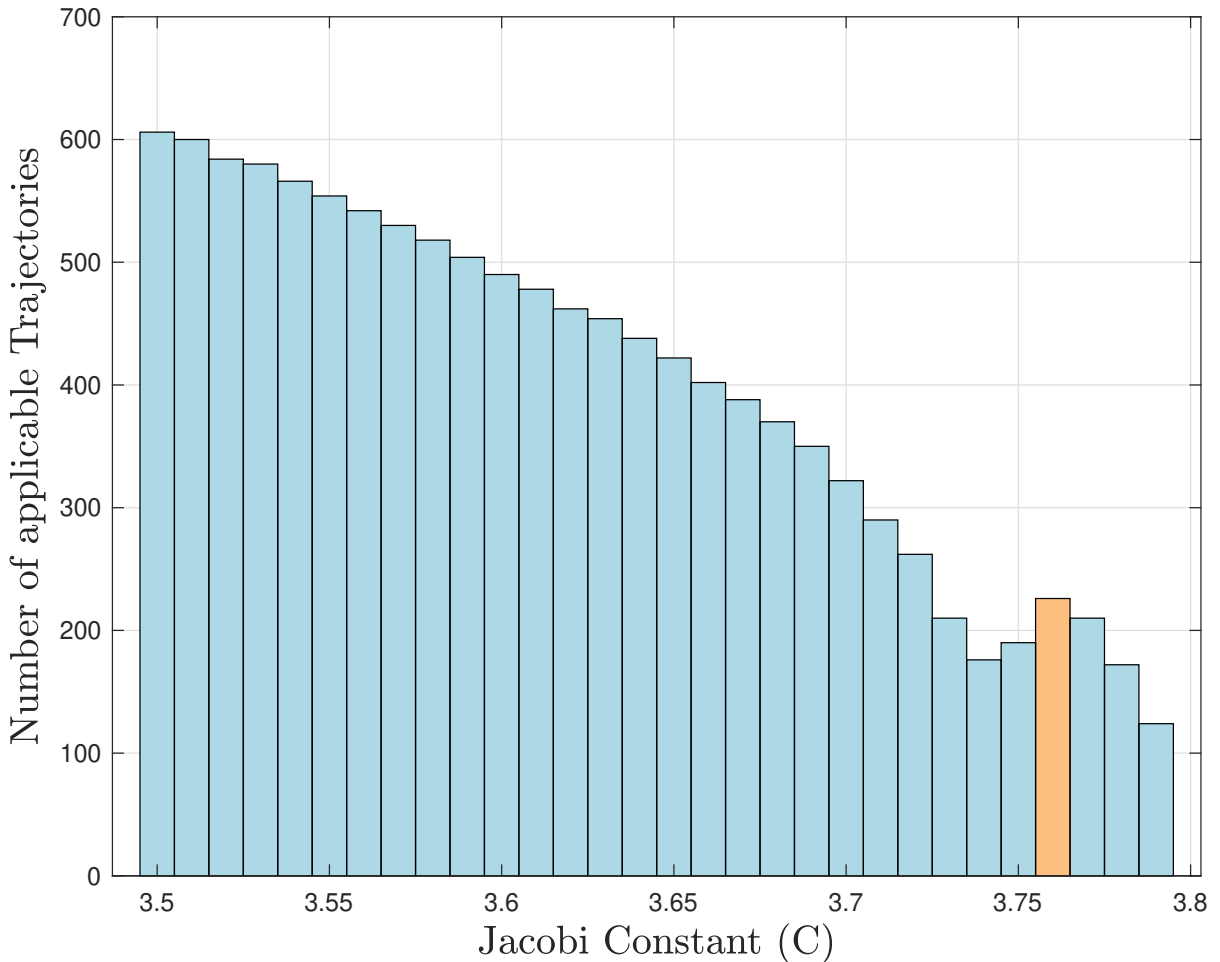
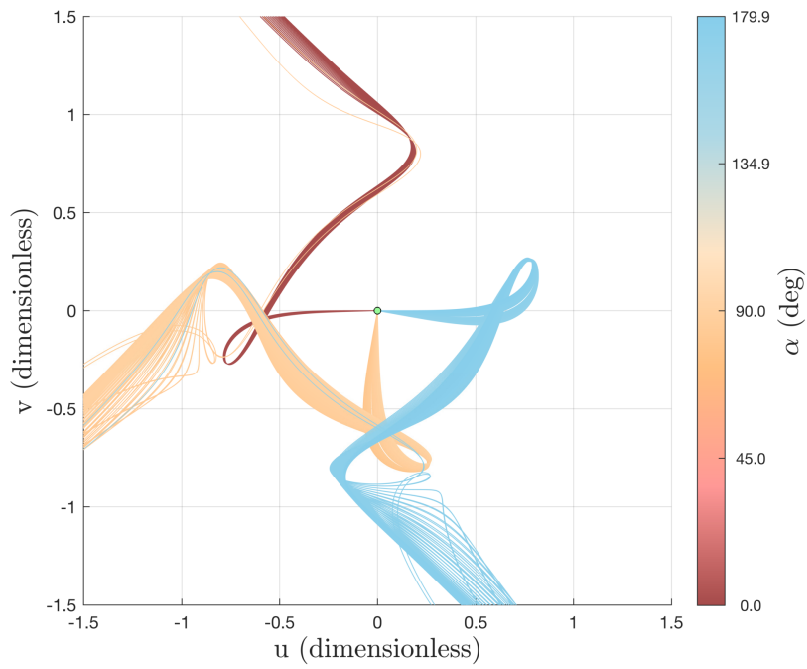


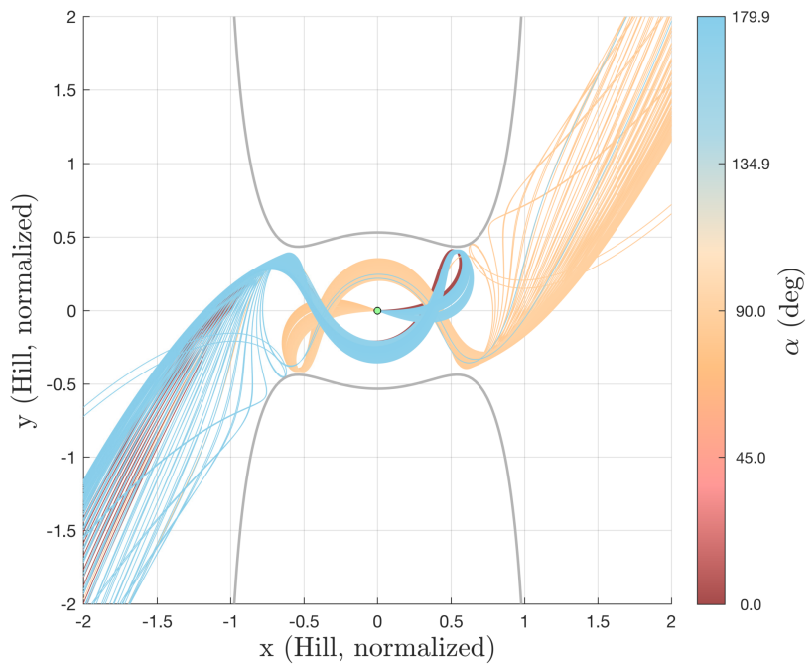
Figure 4: Number of applicable trajectories as a function of the Jacobi constant

Figure 5 illustrates the applicable trajectories corresponding to $C = 3.76$ in the regularized $u - v$ plane and the Hill plane for different α values. While α in the regularized frame is angle without a significant physical meaning, it is utilized herein for identifying each trajectory. Both the regularized and Hill coordinates provide general solutions for the HCR3BP, independent of the Mars-Deimos system properties.

To weigh in the physical properties of the Mars-Deimos system, we establish an additional reference frame called the Deimos Rotating Frame (DRF). This frame clearly



(a) $u - v$ coordinates



(b) Hill normalized coordinates

Figure 5: applicable trajectories for $C = 3.76$

illustrates the trajectories by employing the physical parameters of the system given in Table. 2. In this frame, we have

$$\hat{X} = a\mu^{\frac{1}{3}}\hat{x} \approx 30.72\hat{x} \text{ km} \quad (19a)$$

$$\hat{Y} = a\mu^{\frac{1}{3}}\hat{y} \approx 30.72\hat{y} \text{ km} \quad (19b)$$

Figure 6 depicts the collision trajectories in DRF for $C = 3.76$. For this plot, Deimos' mean radius, listed in Table 2, was taken into account.

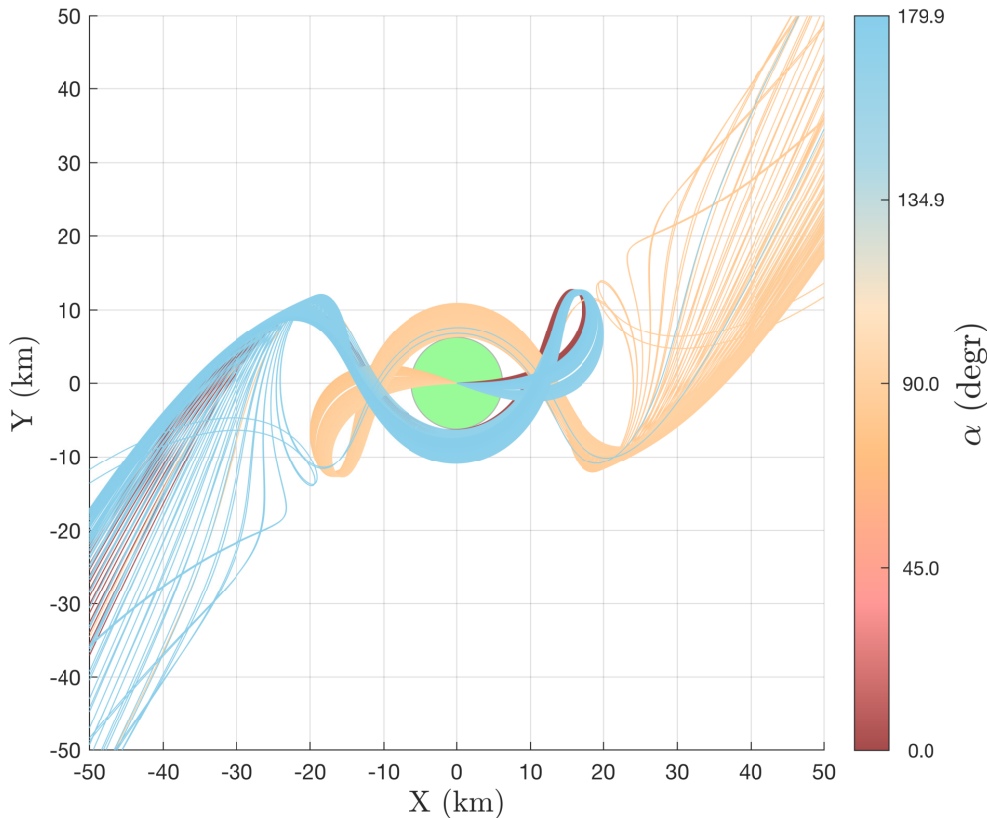


Figure 6: applicable trajectories in the Deimos rotating frame for $C = 3.76$.

3.2 Poincaré Map

A Poincaré map constitutes an essential tool in the analysis of dynamical systems, as it reduces the continuous flow into a discrete map. This is accomplished by designating a lower-dimensional SoS, and tracking the sequence of points where trajectories repeatedly intersect. The geometric pattern formed by these intersection points discloses the underlying dynamics, distinguishing between periodic, quasiperiodic, and chaotic behaviors. Moreover, this map offers the phase distribution of intersecting trajectories, enabling the isolation of the region in phase space wherein collision trajectories occur. In the current

endeavor, we use the same numerical integration scheme described previously (cf. Table 1) to compute the Poincaré map for several SoS of interest.

We define two subspaces in the four-dimensional phase-space of the system (x, y, \dot{x}, \dot{y}) :

$$\mathbb{R}_1^3 : (x, y, \dot{y}), \quad \mathbb{R}_2^3 : (x, y, \dot{x}) \quad (20)$$

The procedure includes a numerical Poincaré map generation for the Hill problem with a Jacobi constant of $C = 3.76$. It generates 1800 trajectories by integrating the regularized equations of motion, Eq. (13) backward in time from collision initial conditions, recording the intersection points with five predefined surfaces at

$$x_i = \left\{ -1, -\left(\frac{1}{3}\right)^{\frac{1}{3}}, 0, \left(\frac{1}{3}\right)^{\frac{1}{3}}, 1 \right\}, \quad (21)$$

for each of the predefined subspaces given by Eq. (20). The list of the complete set of SoS is given by

$$\Sigma_{\dot{y}}^{-1} : (-1, y, \dot{y}) \in \mathbb{R}_1^3 \quad \Sigma_{\dot{x}}^{-1} : (-1, x, \dot{x}) \in \mathbb{R}_2^3 \quad (22a)$$

$$\Sigma_{\dot{y}}^{-\left(\frac{1}{3}\right)^{\frac{1}{3}}} : \left(-\left(\frac{1}{3}\right)^{\frac{1}{3}}, y, \dot{y} \right) \in \mathbb{R}_1^3 \quad \Sigma_{\dot{x}}^{-\left(\frac{1}{3}\right)^{\frac{1}{3}}} : \left(-\left(\frac{1}{3}\right)^{\frac{1}{3}}, x, \dot{x} \right) \in \mathbb{R}_2^3 \quad (22b)$$

$$\Sigma_{\dot{y}}^0 : (0, y, \dot{y}) \in \mathbb{R}_1^3 \quad \Sigma_{\dot{x}}^0 : (0, x, \dot{x}) \in \mathbb{R}_2^3 \quad (22c)$$

$$\Sigma_{\dot{y}}^{\left(\frac{1}{3}\right)^{\frac{1}{3}}} : \left(\left(\frac{1}{3}\right)^{\frac{1}{3}}, y, \dot{y} \right) \in \mathbb{R}_1^3 \quad \Sigma_{\dot{x}}^{\left(\frac{1}{3}\right)^{\frac{1}{3}}} : \left(\left(\frac{1}{3}\right)^{\frac{1}{3}}, x, \dot{x} \right) \in \mathbb{R}_2^3 \quad (22d)$$

$$\Sigma_{\dot{y}}^1 : (1, y, \dot{y}) \in \mathbb{R}_1^3 \quad \Sigma_{\dot{x}}^1 : (1, x, \dot{x}) \in \mathbb{R}_2^3 \quad (22e)$$

The algorithm visualizes the phase-space by generating two-dimensional Poincaré maps (y - \dot{y} and y - \dot{x}) and a three-dimensional representation of the trajectories in phase space with points color-coded, corresponded to α , which serves as an identification for each trajectory. Figure 7 illustrates the arrangement in the phase space for each SoS. Figure 7a displays $\Sigma_{\dot{y}}^{x_i} \in \mathbb{R}_1^3$ and, Figure 7b presents the configuration of $\Sigma_{\dot{x}}^{x_i} \in \mathbb{R}_2^3$. The following Figures depict the Poincaré map in each one of the following SoS: Figure 8 shows the Poincaré map at $\Sigma_{\dot{y}}^{-1}$ and $\Sigma_{\dot{x}}^{-1}$; Fig. 9 shows the Poincaré map at $\Sigma_{\dot{y}}^{-\left(\frac{1}{3}\right)^{\frac{1}{3}}}$ and $\Sigma_{\dot{x}}^{-\left(\frac{1}{3}\right)^{\frac{1}{3}}}$; Fig. 10 shows the Poincaré map at $\Sigma_{\dot{y}}^0$ & $\Sigma_{\dot{x}}^0$; Fig. 11 shows the Poincaré map at $\Sigma_{\dot{y}}^{\left(\frac{1}{3}\right)^{\frac{1}{3}}}$ and $\Sigma_{\dot{x}}^{\left(\frac{1}{3}\right)^{\frac{1}{3}}}$; and Fig. 12 shows the Poincaré map at $\Sigma_{\dot{y}}^1$ and $\Sigma_{\dot{x}}^1$.

Each figure illustrates the density of initial conditions on a given SoS that result in collision trajectories with the secondary. By identified the dense regions in each map, one can determine which trajectories are less sensitive to small perturbations, thus rendering those trajectories more robust.

The inherent symmetries of the Hill problem (Eqs. (9)) result in a distinct anti-symmetry across the Poincaré maps. This behavior is demonstrated by comparing Fig. 8

to Fig. 12, and Fig. 9 to Fig. 11. The central region, shown in Fig. 10, also exhibits this characteristic.

4 Minimal Impact-Speed

One may consider several methods to determine a collision trajectory that is optimal in some sense. One consideration involves identifying a trajectory that minimizes the impact speed, ultimately leading to reduced fuel consumption for the final rendezvous maneuver with the secondary, while guaranteeing soft landing. To find the minimal impact-speed trajectory, a linear interpolation was used to find the collision speed in each direction, denoted by \dot{X}, \dot{Y} in the DRF as given in Eq. (19), for each of the applicable trajectories. As previously mentioned, Deimos is highly nonspherical; however, for the purpose of this study, the mean radius of Deimos was used. (cf. Table 2). Subsequently For each one of the trajectories, the impact speed $\|V\| = \sqrt{\dot{X}^2 + \dot{Y}^2}$ was derived.

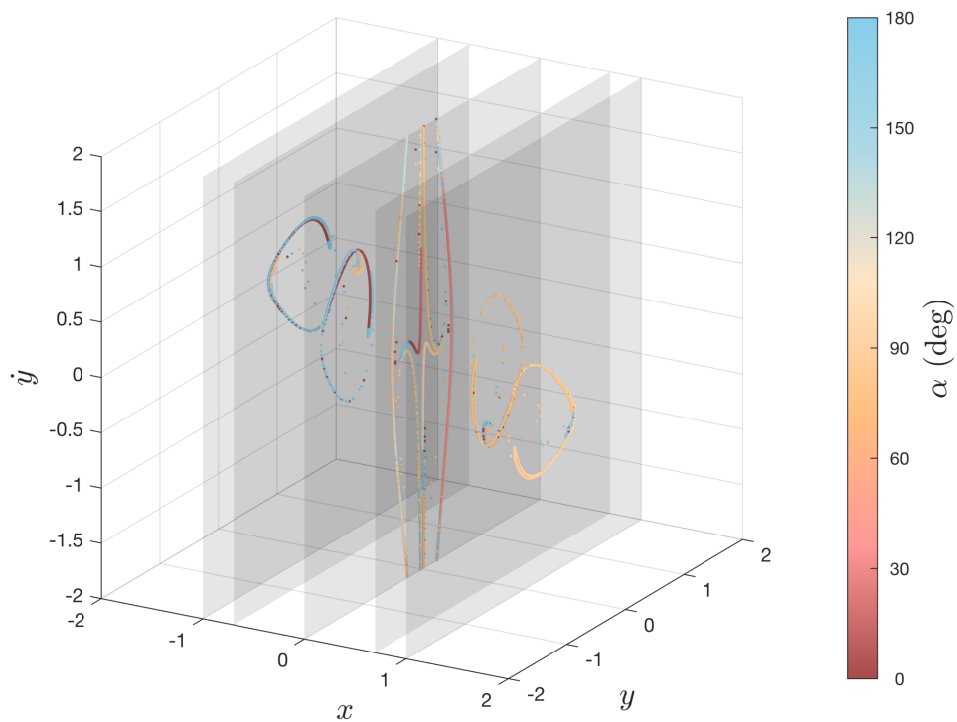
Figure 13 depicts the relationship between α and the impact speed $\|V\|$. It was found that the optimal trajectory in the sense of minimizing the impact speed had an aspect angle $\alpha = 79.7$ deg, and a final speed of $\|V\| = 4.4272$ m/s. Figures 14a, 14b, and 15 depict the trajectory in the regularized $u - v$ coordinates, Hill's coordinates, and the physical rotating frame, respectively.

5 Summary and Conclusions

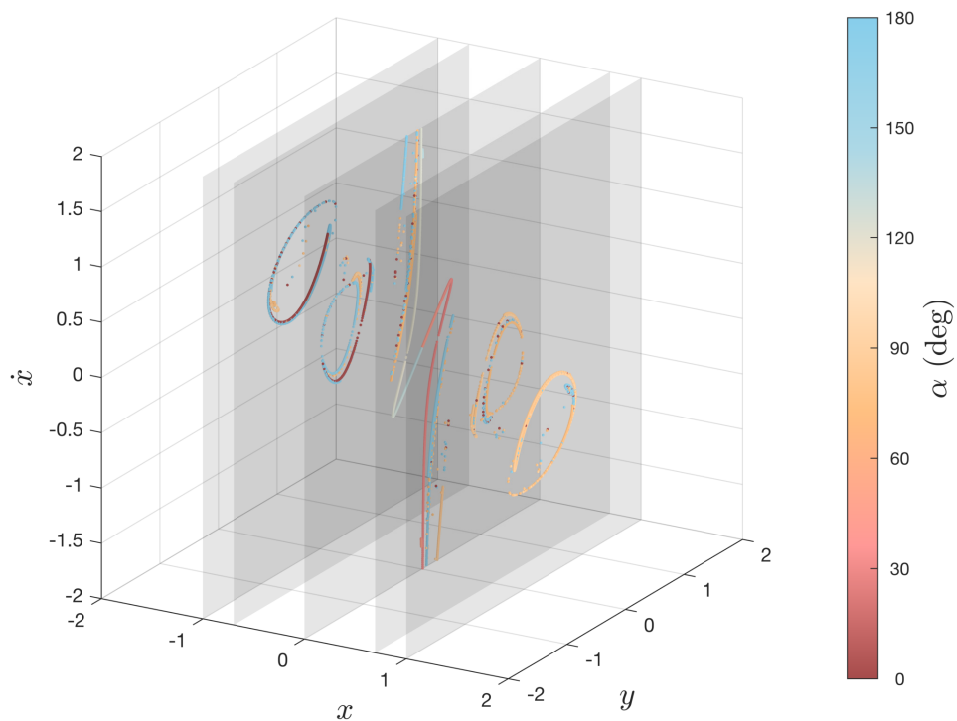
This research found trajectories that collide with the secondary body within the framework of Hill's circular restricted three-body problem (HCR3BP). The study first established the theoretical foundation by reviewing the general Circular Restricted Three-Body Problem (CR3BP) and detailing the assumptions that lead to Hill's formulation of the CR3BP. Subsequently, key properties of the mathematical model were presented and discussed, including the Jacobian integral, equilibrium point and the zero-velocity curves.

In the next part of the investigation, we aimed to numerically determine the collision trajectories. This numerical process involved integrating backwards in a regularized fictitious time variable from the point of collision, in order to identify initial conditions that would lead to a collision with the secondary. The collision orbits we identified were filtered out to include only the physical trajectories (applicable trajectories) that corresponded to the problem statement.

An important conclusion is that the Jacobi integral $C = 3.76$ represents a distinct scenario wherein a relatively small amount of energy leads to numerous collision trajectories. Poincaré maps clearly detect the region in phase-space that generates collision trajectories. In the final section of this investigation, we focused on identifying the optimal trajectory in terms of the Minimal impact velocity for $C = 3.76$. Through the process,

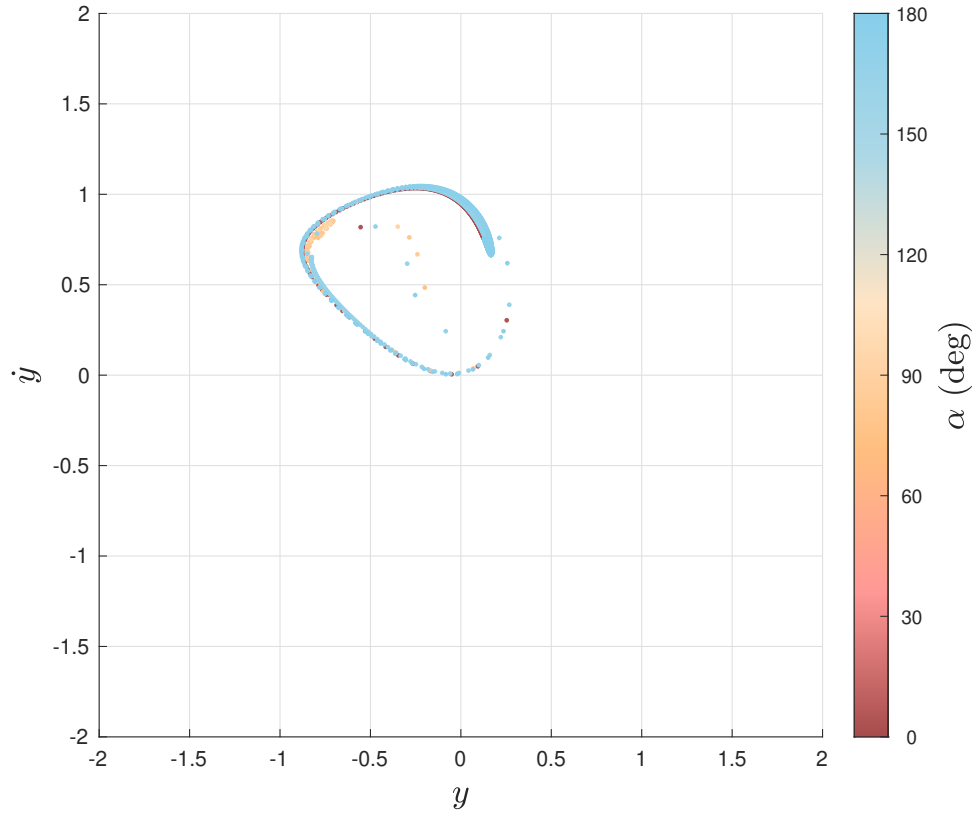


(a) Phase space configuration of $\Sigma_y^{x_i} \in \mathbb{R}_1^3$

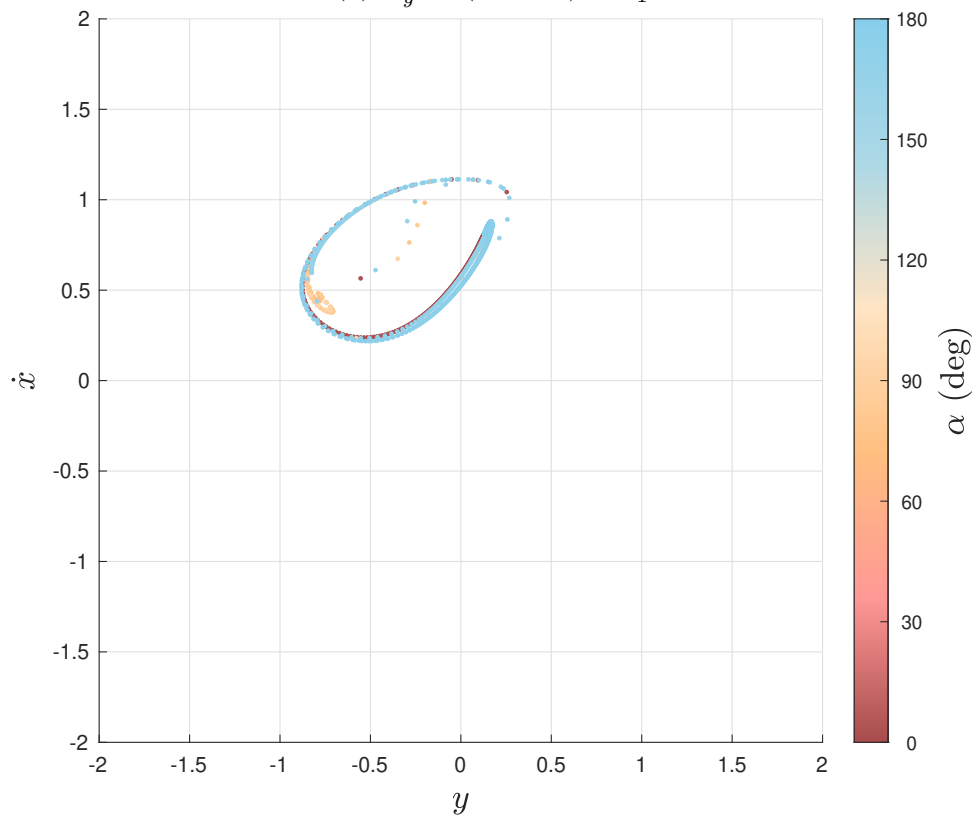


(b) Phase space configuration of $\Sigma_{\dot{x}}^{x_i} \in \mathbb{R}_2^3$

Figure 7: Three-dimensional Poincaré sections for $C = 3.76$.

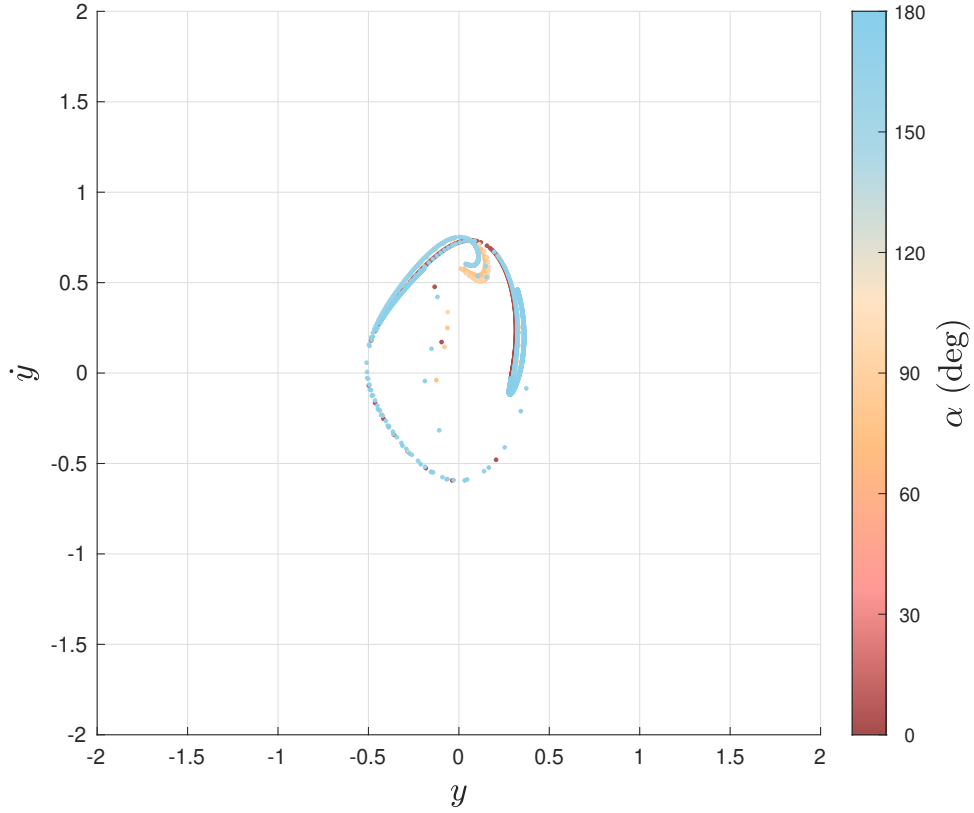


(a) $\Sigma_y^{-1} : (-1, y, \dot{y}) \in \mathbb{R}_1^3$

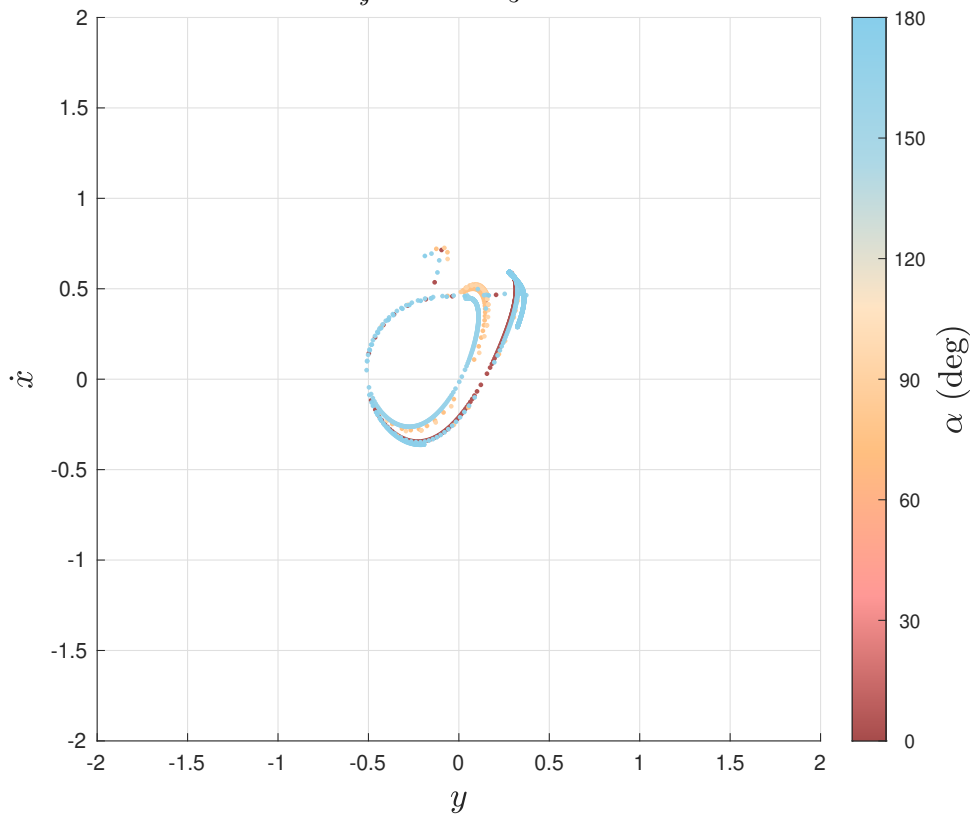


(b) $\Sigma_x^{-1} : (-1, x, \dot{x}) \in \mathbb{R}_2^3$

Figure 8: Poincaré SoS for $x = -1$ and $C = 3.76$ (Σ_y^{-1} & Σ_x^{-1}).

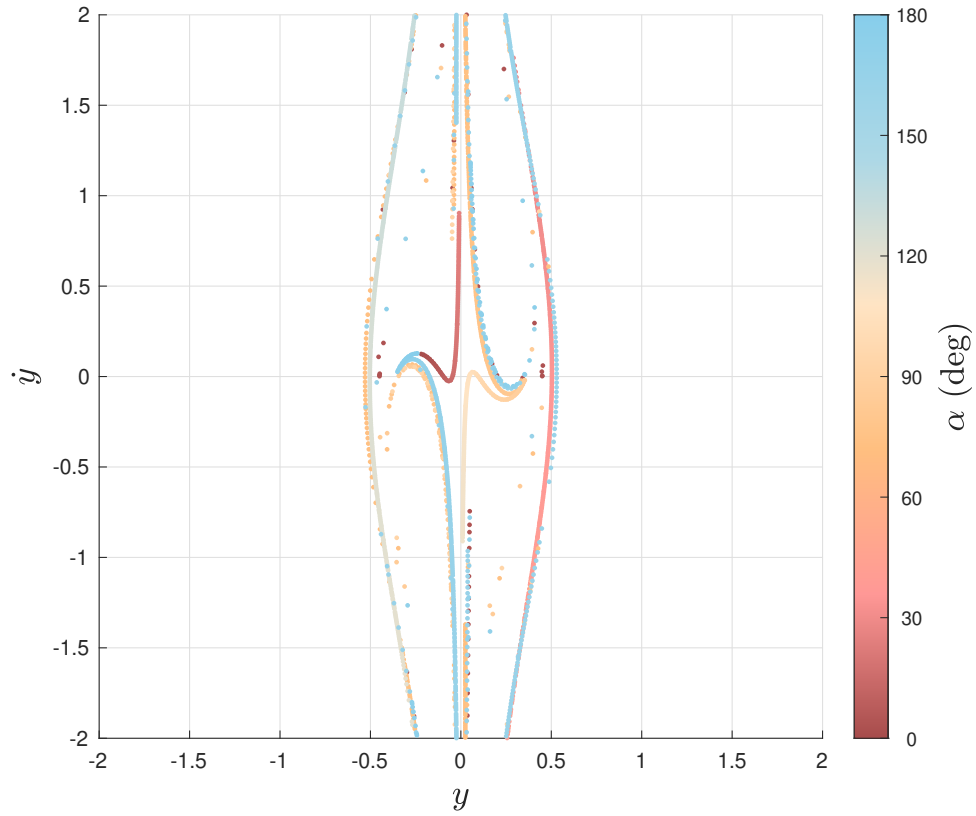


(a) $\Sigma_{\dot{y}}^{-\left(\frac{1}{3}\right)^{\frac{1}{3}}} : \left(-\left(\frac{1}{3}\right)^{\frac{1}{3}}, y, \dot{y}\right) \in \mathbb{R}_1^3$

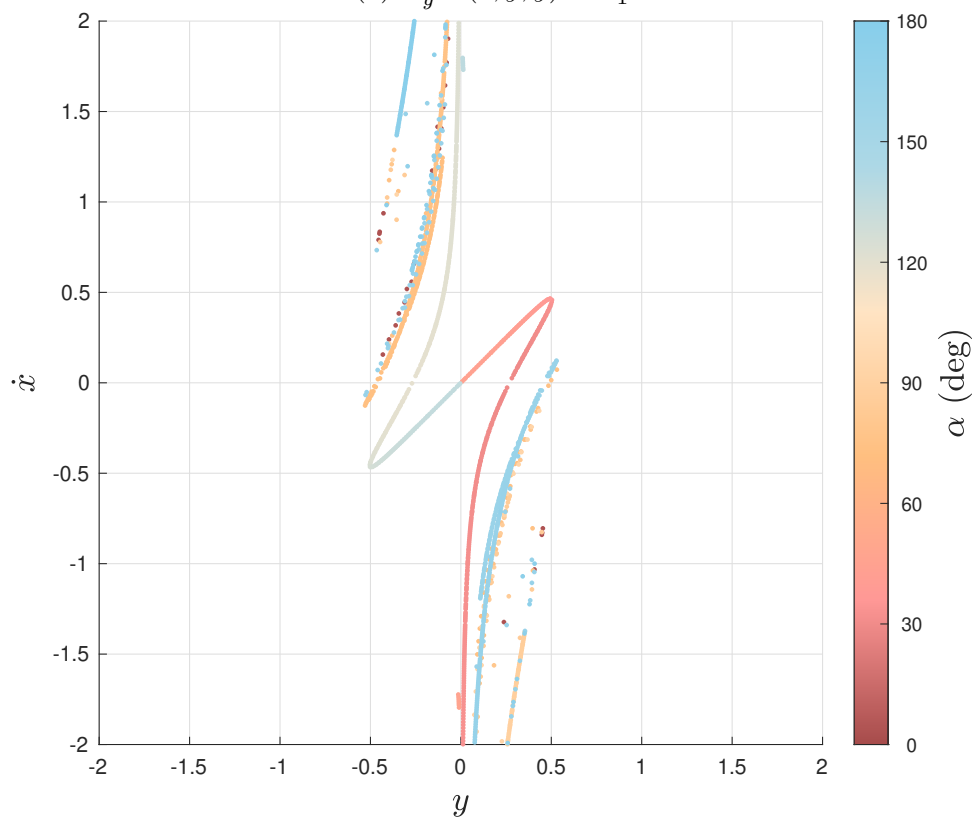


(b) $\Sigma_{\dot{x}}^{-\left(\frac{1}{3}\right)^{\frac{1}{3}}} : \left(-\left(\frac{1}{3}\right)^{\frac{1}{3}}, y, \dot{x}\right) \in \mathbb{R}_2^3$

Figure 9: Poincaré SoS for $x = -\left(\frac{1}{3}\right)^{\frac{1}{3}}$ and $C = 3.76$.

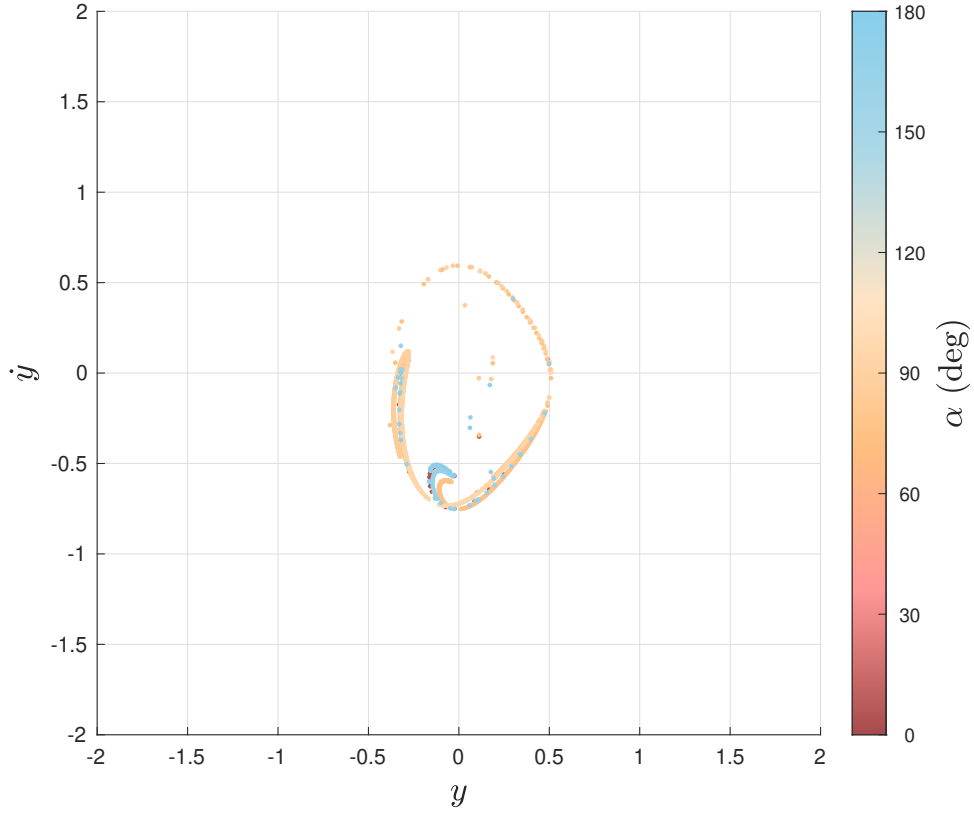


(a) $\Sigma_y^0 : (0, y, \dot{y}) \in \mathbb{R}_1^3$

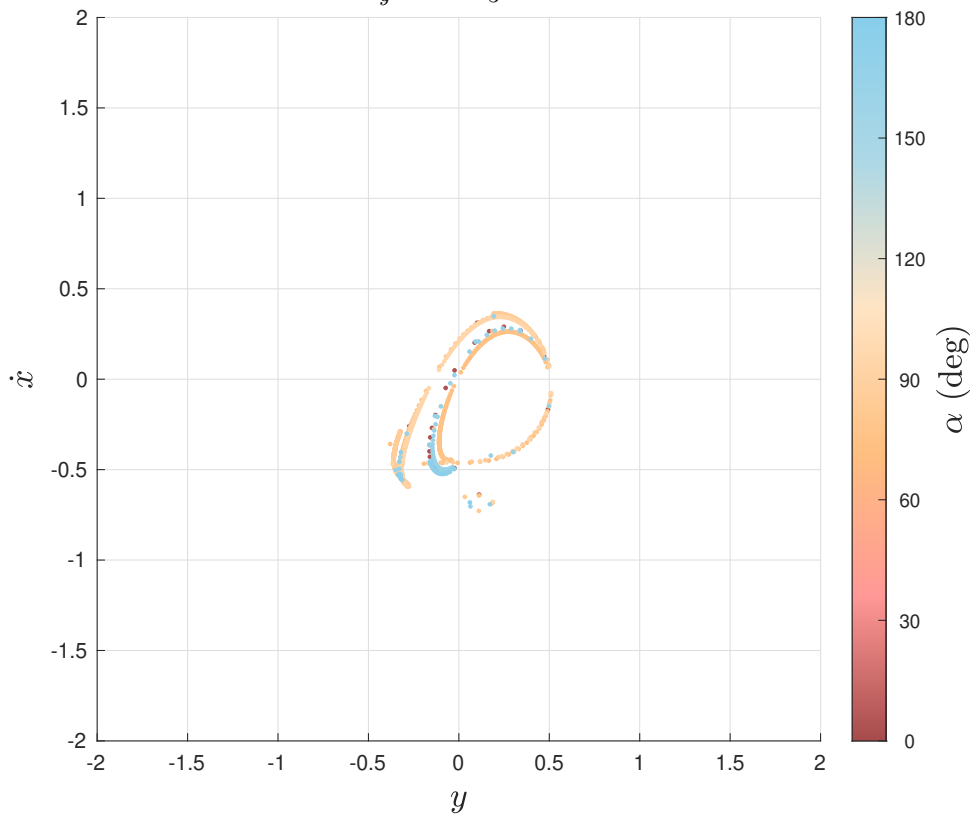


(b) $\Sigma_x^0 : (0, x, \dot{x}) \in \mathbb{R}_2^3$

Figure 10: Poincaré SoS for $x = 0$ and $C = 3.76$.

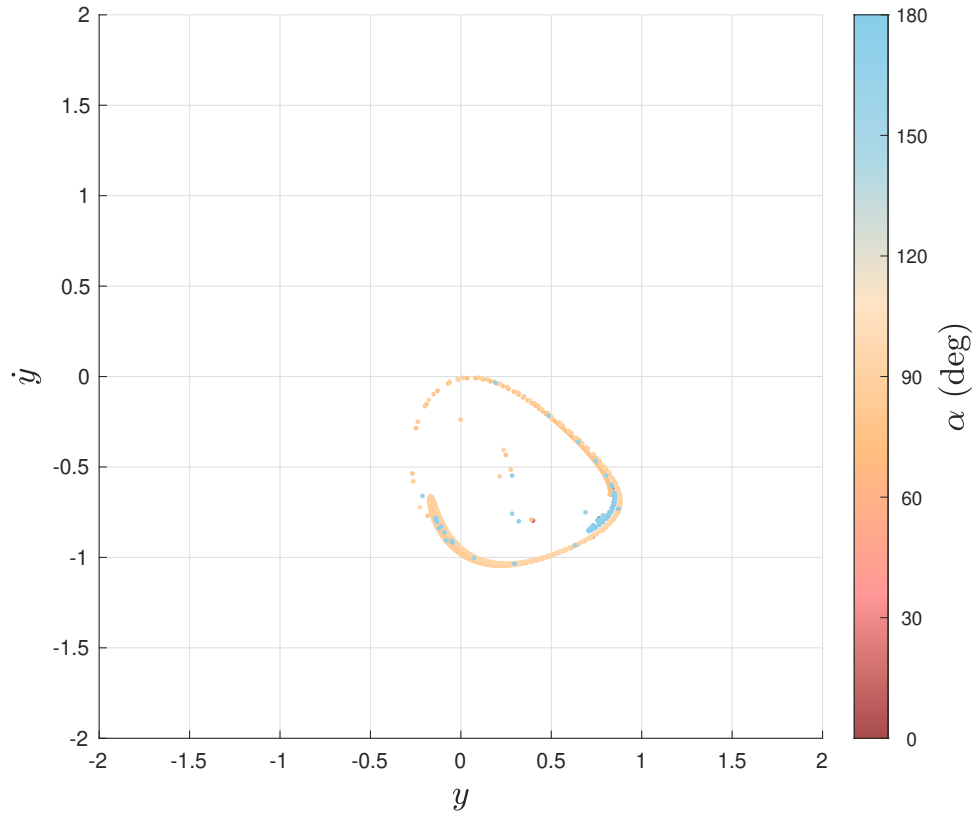


(a) $\Sigma_{\dot{y}}^{(\frac{1}{3})^{\frac{1}{3}}} : ((\frac{1}{3})^{\frac{1}{3}}, y, \dot{y}) \in \mathbb{R}_1^3$

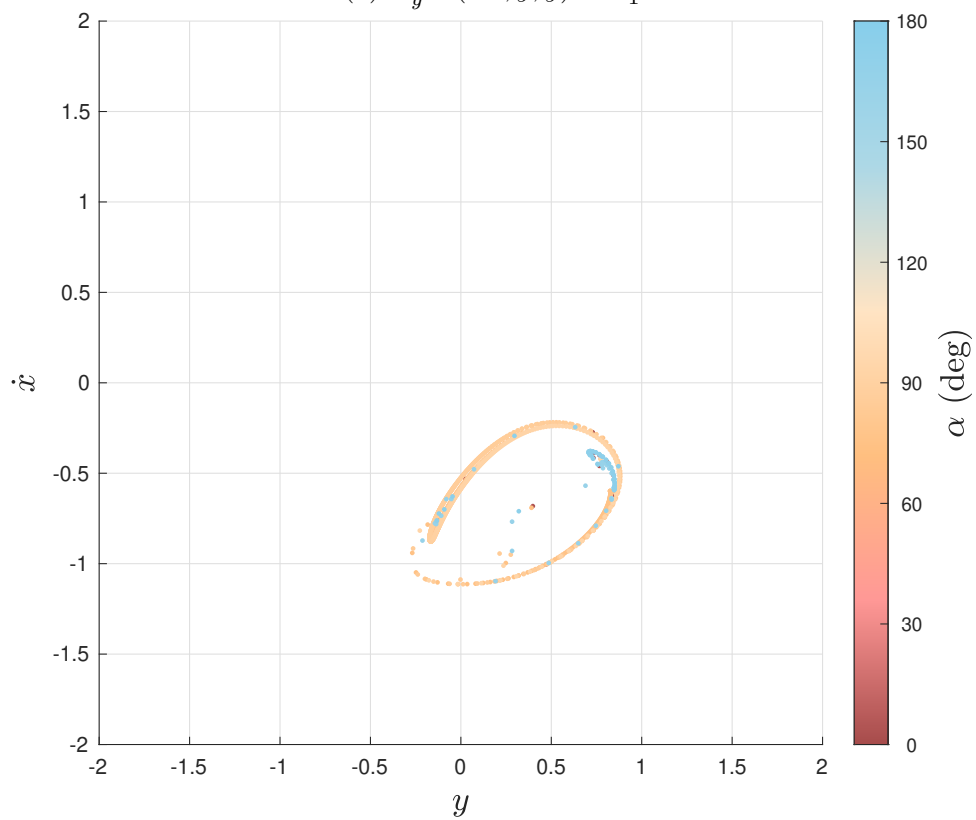


(b) $\Sigma_{\dot{x}}^{-(\frac{1}{3})^{\frac{1}{3}}} : (-(\frac{1}{3})^{\frac{1}{3}}, y, \dot{x}) \in \mathbb{R}_2^3$

Figure 11: Poincaré SoS for $x = (\frac{1}{3})^{\frac{1}{3}}$ and $C = 3.76$.



(a) $\Sigma_y^1 : (-1, y, \dot{y}) \in \mathbb{R}_1^3$



(b) $\Sigma_x^1 : (1, x, \dot{x}) \in \mathbb{R}_2^3$

Figure 12: Poincaré SoS for $x = 1$ and $C = 3.76$.

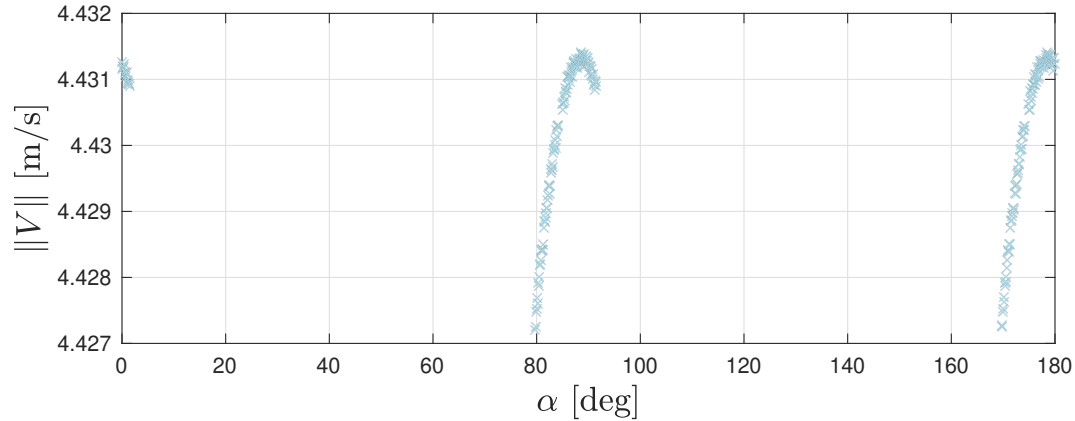


Figure 13: α as a function of the Impact speed for $C = 3.76$.

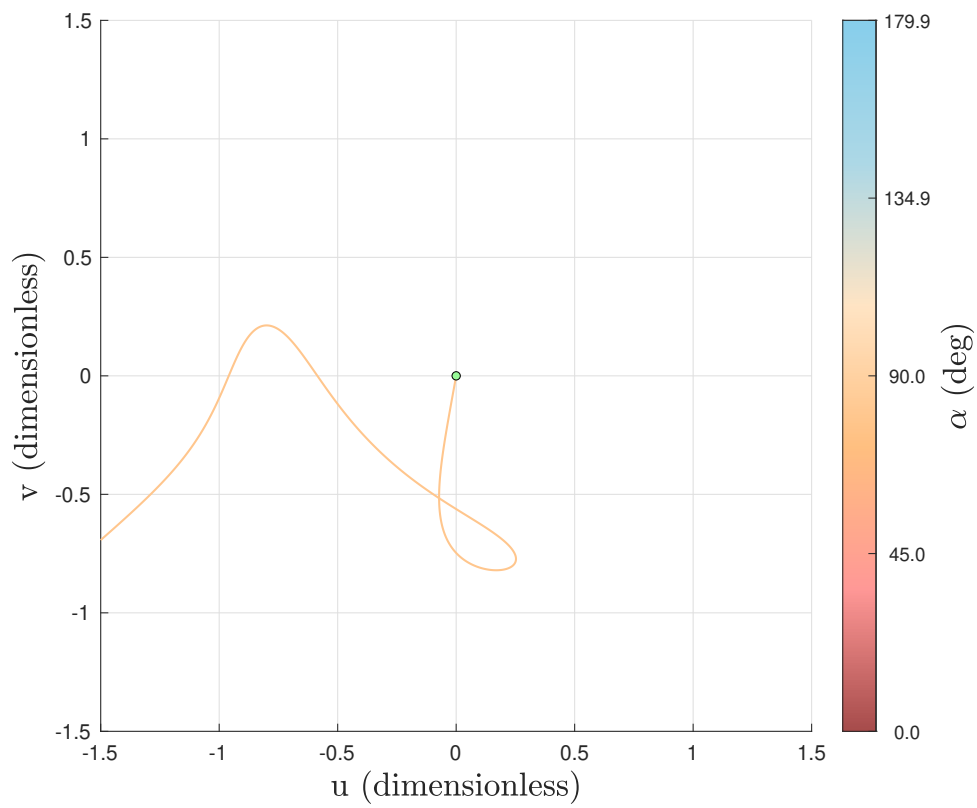
we successfully identified that $\alpha = 79.7$ deg, results in a final velocity of $\|V\| = 4.4272 \frac{m}{s}$, which was the lowest impact velocity for the entire applicable subset of trajectories.

6 Future Work

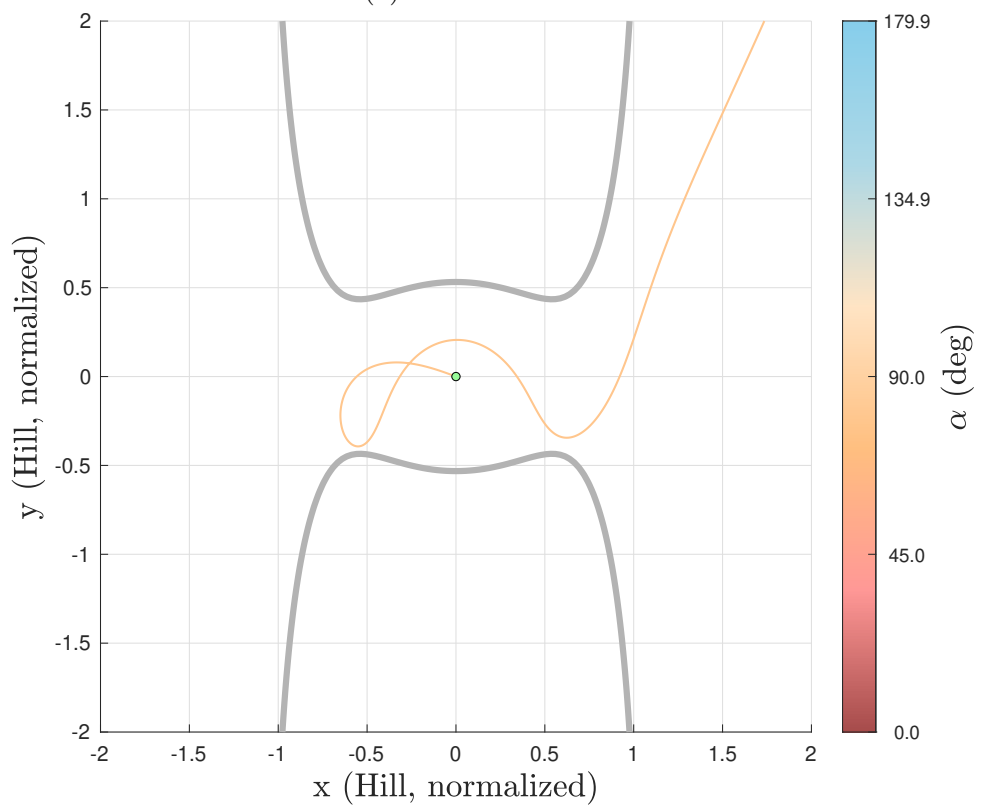
Future work will incorporate more realistic dynamics, taking into an account the effects of the solar radiation pressure, the oblateness of Mars, and the highly-nonspherical shape of Deimos. Another possible study is to extend the analysis to three dimensions. Moreover, future work will identify the optimal trajectory in terms of minimizing sensitivity to initial conditions using global search algorithms (e.g. Genetic Algorithms). Finally, low-thrust closed-loop guidance laws, suitable for steering a spacecraft onto soft landing collision trajectories based on the identified optimal trajectory, will be designed, enabling autonomous landing on the Martian moon.

References

- [1] Wolfgang Osterhage. *Johannes Kepler : the order of things*. Springer Biographies. Springer, Cham, 1 edition, 2020.
- [2] RP Boas Jr. James r. newman, the world of mathematics. 1957.
- [3] Sylvio R Bistafa. On the rectilinear motion of three bodies mutually attracting each other. *Euleriana*, 1(2):188–196, August 2021.
- [4] Joseph-Louis Lagrange. Essai sur le probleme des trois corps. *Prix de l'académie royale des Sciences de paris*, 9:292, 1772.
- [5] Carl GJ Jacobi. Sur le mouvement d'un point et sur un cas particulier du probleme des trois corps. *Compt. Rend.*, 3:59–61, 1836.



(a) $u - v$ coordinates



(b) Hill normalized plane

Figure 14: Minimal impact trajectory in normalized coordinates

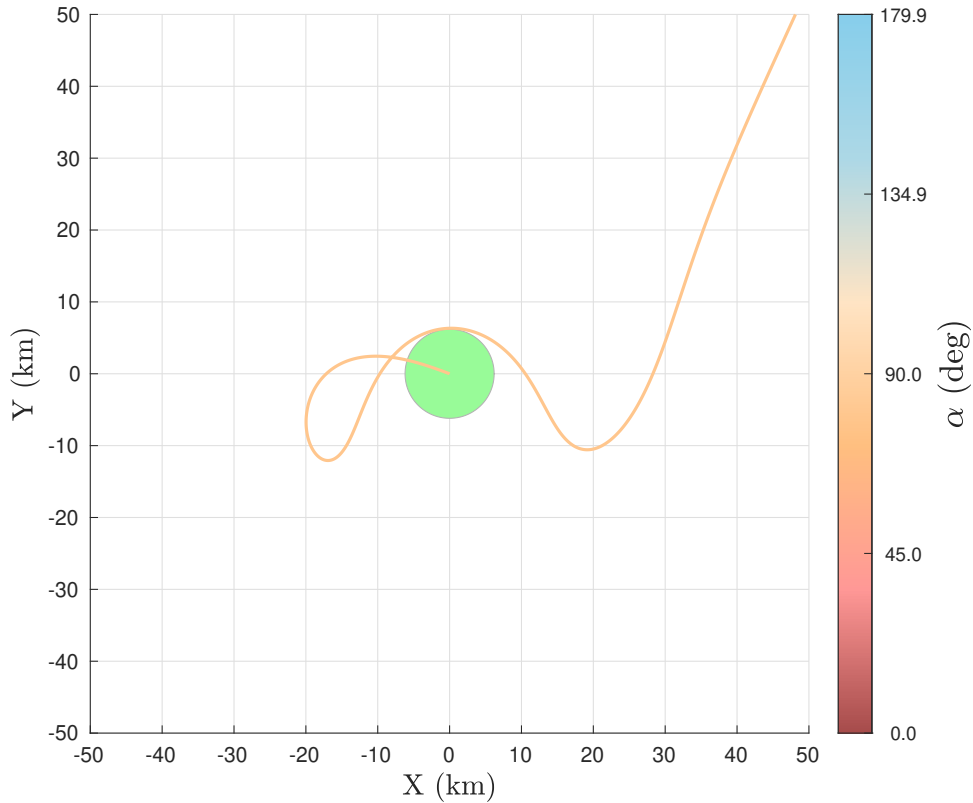


Figure 15: Minimal impact-speed trajectory in the physical Deimos-centered rotating frame

- [6] George William Hill. On the part of the motion of the lunar perigee which is a function of the mean motions of the sun and moon. 1886.
- [7] G. W. Hill. Researches in the lunar theory. *American Journal of Mathematics*, 1(1):5–26, 1878.
- [8] Henri Poincaré. *Les méthodes nouvelles de la mécanique céleste*, volume 2. Gauthier-Villars et fils, imprimeurs-libraires, 1893.
- [9] Michel Hénon. Numerical exploration of the restricted problem, v. *Astronomy and Astrophysics*, vol. 1, p. 223-238 (1969)., 1:223–238, 1969.
- [10] Cengiz Aydin and Alexander Batkhin. Studying network of symmetric periodic orbit families of the hill problem via symplectic invariants. *Celestial Mechanics and Dynamical Astronomy*, 137(2):1–77, 2025.
- [11] Michel Henon. New families of periodic orbits in hill’s problem of three bodies. *Celestial Mechanics and Dynamical Astronomy*, 85(3):223–246, 2003.
- [12] C Simó and T de J Stuchi. Central stable/unstable manifolds and the destruction of kam tori in the planar hill problem. *Physica D: Nonlinear Phenomena*, 140(1-2):1–32, 2000.

- [13] VV Markellos, AE Roy, MJ Velgakis, and SS Kanavos. A photogravitational hill problem and radiation effects on hill stability of orbits. *Astrophysics and space science*, 271(3):293–301, 2000.
- [14] VV Markellos, AE Roy, EA Perdios, and CN Douskos. A hill problem with oblate primaries and effect of oblateness on hill stability of orbits. *Astrophysics and space science*, 278(3):295–304, 2001.
- [15] A. E. Perdiou, E. A. Perdios, and V. S. Kalantonis. Periodic orbits of the hill problem with radiation and oblateness. *Astrophysics and Space Science*, 342(1):19–30, June 2012.
- [16] Michel Hénon. Numerical exploration of the restricted problem. vi. hill’s case: Non-periodic orbits. *Astronomy and Astrophysics, Vol. 9, p. 24-36*, 9:24–36, 1970.
- [17] Pini Gurfil, N. Jeremy Kasdin, and Egemen Kolemen. Hamilton–jacobi modelling of stellar dynamics. *Advances in Space Research*, 36(6):1143–1150, 2005. Infrared/Submm Astronomy from Space.
- [18] Eray Demir. Ejection-collision orbits in the modified hill’s problem. Master’s thesis, Universitat Politècnica de Catalunya, 2019.
- [19] Charles C Conley. Low energy transit orbits in the restricted three-body problems. *SIAM Journal on Applied Mathematics*, 16(4):732–746, 1968.
- [20] B. F. Villac and D. J. Scheeres. Escaping trajectories in the hill three-body problem and applications. *Journal of Guidance, Control, and Dynamics*, 26(2):224–232, March 2003.
- [21] Pini Gurfil. Unified approach to far-range space rendezvous. *Advances in Space Research*, 76(3):1662–1673, August 2025.
- [22] Marina Brozović, Robert A. Jacobson, and Ryan S. Park. Revised ephemerides of the martian satellites, phobos and deimos. *The Astronomical Journal*, 170(1):42, June 2025.
- [23] S. Nagai, H. Senshu, K. Matsumoto, N. Namiki, and N. Hirata. High-resolution shape models of phobos and deimos from the combination of stereophotoclinometry and the gaskell method. *Earth, Planets and Space*, 75(103):1–14, 2023.
- [24] Aili McConnon. Latest values of fundamental physics constants. *Scilight*, 2021(39), September 2021.
- [25] Kiyoshi Kuramoto. Origin of phobos and deimos awaiting direct exploration. *Annual Review of Earth and Planetary Sciences*, 52(1):495–519, July 2024.

- [26] Ariel N. Deutsch, James W. Head, Kenneth R. Ramsley, Carle M. Pieters, Ross W.K. Potter, Ashley M. Palumbo, Michael S. Bramble, James P. Cassanelli, Erica R. Jawin, Lauren M. Jozwiak, Hannah H. Kaplan, Connor F. Lynch, Alyssa C. Pascuzzo, Le Qiao, and David K. Weiss. Science exploration architecture for phobos and deimos: The role of phobos and deimos in the future exploration of mars. *Advances in Space Research*, 62(8):2174–2186, October 2018.
- [27] William Pratt and Joshua Hopkins. Comparison of deimos and phobos as destinations for human exploration and identification of preferred landing sites. In *AIAA SPACE 2011 Conference and Exposition*. American Institute of Aeronautics and Astronautics, June 2011.
- [28] Alessandra Celletti. Basics of regularization theory. In *Chaotic worlds: from order to disorder in gravitational N-body dynamical systems*, pages 203–230. Springer, 2003.
- [29] Victor G. Szebehely. *Theory of orbit : the restricted problem of three bodies / Victor Szebehely*. Academic Press, New York, 1967.
- [30] Mauri J Valtonen and Hannu Karttunen. *The three-body problem*. Cambridge University Press, 2006.
- [31] Kenneth R. Meyer and Dieter S. Schmidt. Hill’s lunar equations and the three-body problem. *Journal of Differential Equations*, 44(2):263–272, May 1982.
- [32] JUAN J. MORALES-RUIZ, CARLES SIMÓ, and SERGI SIMON. Algebraic proof of the non-integrability of hill’s problem. *Ergodic Theory and Dynamical Systems*, 25(4):1237–1256, 2005.
- [33] K. E. PAPADAKIS. The planar photogravitational hill problem. *International Journal of Bifurcation and Chaos*, 16(06):1809–1821, June 2006.
- [34] James H Verner. Numerically optimal runge–kutta pairs with interpolants. *Numerical Algorithms*, 53(2):383–396, 2010.